

Supplementary Material: Separability of drag and thrust in undulatory animals and machines

Rahul Bale,^{1,+} Anup A. Shirgaonkar,^{1,+} Izaak D. Neveln,² Amneet Pal Singh Bhalla,¹

Malcolm A. MacIver,^{1,2,3,*} and Neelesh A. Patankar^{1,*}

1 Department of Mechanical Engineering, Northwestern University,

2 Department of Biomedical Engineering, Northwestern University,

3 Department of Neurobiology, Northwestern University,

2145 Sheridan Road, Evanston, IL 60208, USA

+ Authors made equal contributions

* Authors for correspondence (n-patankar@northwestern.edu, maciver@northwestern.edu)

S1 Difference between this work and Lighthill's approach

Our approach is different from prior work by Lighthill [1–3] for the following reasons: **1)** Our kinematic decomposition ensures that the realizability condition D2 (the decomposed body movements should be such that the surface of the body will move in a continuous fashion so that the kinematics can be realized in experiments or simulations) is satisfied, unlike Lighthill's decomposition. Thus, our decomposition allows setting up independent sets of simulations/experiments to determine the drag and thrust components. **2)** We show that the force condition D3 (the sum of the drag and thrust forces from the decomposed body movements must be equal to the force due the original body movement of the swimmer) is satisfied based on our approach. Because Lighthill's approach did not satisfy condition D2, this verification has not been possible. **3)** We are able to estimate both thrust and drag, unlike Lighthill's work where appropriate drag estimates are not available. Lighthill's approach for the decomposition of drag and thrust is summarized below.

Consider a generic surface with a traveling wave as shown in Fig. S1. It could represent the body of a swimmer or the surface of a fin. Consider the wave to have a constant amplitude and that the wave is traveling from left to right (i.e. backward) with velocity U_w which is constant. Due to the wave motion, any point on the surface oscillates laterally (or oscillates laterally along a figure eight-shaped path if the body is assumed inextensible [1]) with velocity $V_w = -2\pi f A \sin[2\pi(x/\lambda - ft)]$, where A is the amplitude of the wave, f is the frequency, x is the axial location of the point, and λ is the wavelength. It follows that

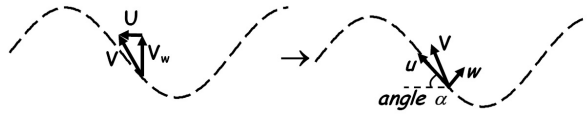


Figure S1. Lighthill [1] decomposed the resultant velocity V at a point on the surface into a component u tangential to it (causing resistive drag) and a component w normal to it (causing reactive thrust).

$U_w = \lambda f$. Let U be the forward translational velocity (i.e. to the left; Fig. S1) of the surface as a whole and let the surrounding fluid be stationary. Positive values of U_w will imply a backward traveling wave whereas positive values of U imply a forward translating surface. The resultant velocity at any point on the surface is V as shown in Fig. S1. Lighthill [2] considered the components of V that are tangential (u) and normal (w) to the surface of the wave with large amplitude oscillations. It can be shown that

$$w = (U_w - U) \sin[\alpha], \quad (\text{S1})$$

$$u = \frac{U_w}{\cos[\alpha]} - (U_w - U) \cos[\alpha], \quad (\text{S2})$$

where α is the angle as shown in Fig. S1. Lighthill [2] then stated that the added mass due to the normal component w will be large and therefore it will primarily contribute to the so-called “reactive” force. The axial component of this reactive force was termed thrust. He stated that the tangential component u will have only small contribution to the added mass and thus it will contribute predominantly to the viscous resistance. The axial component of the viscous force was termed drag. In this way, Lighthill formulated the decomposition of the force on the fin into drag- and thrust-causing mechanisms in spite of nonlinearities at high Reynolds numbers. Note that the decomposition of the fin velocity into u and w does not satisfy the realizability condition D2. Lighthill developed expressions to obtain the reactive thrust due to w for elongated bodies or fins [2, 3]. Since thrust T was assumed to be caused by w , according to equation S1, it is a function of $U_w - U$ [3]. The thrust is directed in the forward direction, as desired, when $U_w - U > 0$, whereas it is directed backward when $U_w - U < 0$. According to Lighthill, drag must be a function of U_w and $(U_w - U)$ since it is caused by u (equation S2). However, no expressions for drag were developed.

As shown in Fig. 3 of the Manuscript (figures with numbers that do not have the prefix S are figures of the Manuscript, hereafter this will not be explicitly mentioned) and Table S1, below, the decomposition

proposed in this work is different from Lighthill's. The velocities u_s and u_f that are tangential to the wave surface in our slithering and frozen fin modes, respectively, are given by

$$u_s = U_w / \cos[\alpha], \quad (\text{S3})$$

$$u_f = -(U_w - U) \cos[\alpha]. \quad (\text{S4})$$

The tangential velocity in the slithering mode according to equation S3 corresponds only to the first part of the tangential velocity u according to Lighthill's decomposition in equation S2. The tangential velocity in our frozen fin mode (equation S4) corresponds to the second part of the tangential velocity u in equation S2. The normal velocity in the slithering mode is zero whereas that in the frozen fin mode w_f is given by

$$w_f = (U_w - U) \sin[\alpha], \quad (\text{S5})$$

This normal velocity is the same as w in equation S1. Thus, our results suggest that part of the tangential velocity u in the decomposition of Lighthill [2] that depends on $(U_w - U)$ is in fact coupled with the normal component to account for the thrust force according to the frozen fin mode.

In our decomposition the drag force is a function of U_w unlike the consequence of Lighthill's decomposition where the drag force is expected to be a function of U_w and $(U_w - U)$. The thrust force in our case is a function of $(U_w - U)$ like Lighthill but it has an additional contribution from the tangential

	Lighthill	Current Study
Drag	$u = \frac{U_w}{\cos[\alpha]} - (U_w - U) \cos[\alpha]$	$u_s = \frac{U_w}{\cos[\alpha]}$
Thrust	$w = (U_w - U) \sin[\alpha]$	$w_f = (U_w - U) \sin[\alpha]$ $u_f = -(U_w - U) \cos[\alpha]$

Table S1. Comparison of Lighthill's kinematic decomposition and the one proposed here.

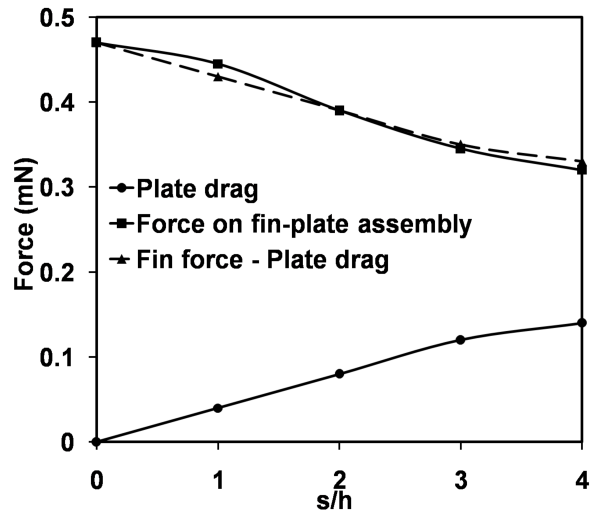


Figure S2. Force F_p on the plate (—●—), force F_{fp} on the fin-plate assembly (—■—), and $F_f - F_p$ (—▲—) as a function of s/h . Agreement between F_{fp} and $F_f - F_p$ shows that there is no momentum enhancement.

velocity along the fin surface.

S2 Optimal height of the ribbon fin: Analysis

S2.1 Swimming velocity

In Fig. 7b we presented the swimming velocity obtained from self-propulsion simulations. In this section we will show that it can also be obtained based on a reduced order model. Doing so will provide insights into the mechanisms underlying the simulation data.

The steady swimming velocity of a self-propelling organism is the one at which the resultant force on the body, averaged over a swimming cycle, is zero. In case of the fin-plate assembly, forces on the plate and the fin are decoupled as seen in Fig. S2. Therefore, at steady swimming $F_f[U_w, U, h] - F_p[U] = 0$, where square brackets indicate “function-of” and U is the translational velocity of the plate-fin assembly. The value of U that satisfies the force equation is the swimming velocity U_s . Only U_w, U and h are the parameters of interest in this analysis. Remaining parameters are assumed to be constant.

According to the drag-thrust decomposition discussed in the Manuscript, $F_f = T_f - D_f$, where T_f and D_f are the thrust and drag forces on the ribbon fin, respectively. It was found that D_f depends on the

wave velocity U_w whereas T_f depends on $(U_w - U)$. Using the drag-thrust decomposition of the force F_f on the fin, the force balance equation for the plate-fin assembly during steady swimming can be written as

$$T_f[U_w - U, h] - D_f[U_w, h] - F_p[U] = 0. \quad (\text{S6})$$

The functions for T_f , D_f , and F_p are obtained as follows. Fig. 4c shows that T_f depends on $(U_w - U)$. A combination of linear and quadratic variations fit the graph well. Since the mechanism of thrust generation is shown to be the low pressure caused by flow separation, thrust is proportional to the effective frontal area of the flapping ribbon fin which scales as h^2 . The drag force D_f is shown to be due to a boundary layer type flow caused by the slithering motion (Fig. 5). It depends on U_w (Fig. 4b), which is a constant in our simulations. The drag force is proportional to the wetted surface area of the ribbon fin which scales as h . Finally, F_p is caused primarily by the boundary layer on the plate. Hence, it is proportional to $U^{3/2}$ (all other parameters are constant). Thus, equation S6 can be written in the following form

$$\{A_1(U_w - U)^2 + A_2(U_w - U)\}h^2 - Bh - CU^{3/2} = 0, \quad (\text{S7})$$

where A_1 , A_2 , B , and C are constants. The term involving h^2 is the thrust force T_f , $D_f = Bh$, and $F_p = CU^{3/2}$. Note that $U_w = 15$ cm/s for all cases considered here. Based on the data in Figures 4b and 4c, we find that $A_1 = 0.0059$ mN-s²/cm⁴, $A_2 = 0.0068$ mN-s/cm³, and $B = 0.51$ mN/cm. We did simulations for flow over a plate and found that $C = 0.017$ mN/(cm/s)^{3/2}. The only unknowns in equation S7 are U and h . Thus, it can be used to obtain the swimming velocity U_s as a function of h .

Analytic solution for U_s : Now we solve the analytic equation S7 and compare it to the swimming velocity computed from self-propulsion simulations of the fin-plate assembly (Fig. 7b). It is possible to obtain an approximate closed form solution for h as a function of U_s by solving equation S7. To do so we note that equation S7 is a quadratic equation for h . Using the quadratic formula for h , keeping the physically relevant solution, and using binomial expansion of a square-root term up to first order, we get the following solution

$$h = \frac{B}{A_1(U_w - U_s)^2 + A_2(U_w - U_s)} + \frac{CU_s^{3/2}}{B}. \quad (\text{S8})$$

The first part on the right hand side corresponds to the swimming of an isolated fin and the second part is the correction due to the drag on the plate. The above equation is solved for U_s and is compared to the

values computed from self-propulsion simulations in Fig. 7b. Also plotted in Fig. 7b is the analytic solution for a hypothetical freely swimming ribbon fin without a plate attached. That solution is obtained from equation S8 by substituting $C = 0$. Below a critical height h_c the analytic swimming velocity becomes negative. Analytic solution in this regime is not plotted since the drag-thrust split model is not valid in this regime. There is no self-propulsion simulation data in this regime since the swimming velocity is very small and the numerical accuracy is not sufficient. The trends in Fig. 7b will be discussed below in two parts: **1)** trends for swimming velocity above the critical fin height, and **2)** swimming at fin heights below the critical value.

1) Fig. 7b shows that, for fin heights above a critical value, the swimming velocity from self-propulsion simulations is in good agreement with the analytic curve for a plate-fin assembly at smaller h and agrees better with the analytic curve for the fin-only case at larger h . This is expected because at h comparable to or larger than the plate height of $s = 2$ cm, the plate drag is dominated by the drag of the ribbon fin. Hence, the plate-fin assembly swims at a velocity that is close to the self-propulsion velocity of the ribbon fin itself. The disagreement between simulated and analytic swimming velocities of the plate-fin assembly, at larger h , arises because the higher-order terms in the binomial expansion were neglected in equation S8.

The key trend of U_s is the rapid rise with respect to h at smaller h and a slow change at larger h . This variation is the primary factor that determines the cost of transport (COT) trends obtained in Fig. 7c. It is clear from Figure 7b that the trend in U_s is inherent to the self-propulsion velocity of the isolated ribbon fin itself. The presence of the plate drag merely plays a role in shifting the swimming velocity to a lower value. Equations S7 and S8 imply that the root cause of the trend in U_s is the fact that the fin thrust T_f scales as h^2 while the fin drag D_f scales as h , and the fact that the swimming velocity affects only T_f . Due to this, at smaller h , any increase in fin height increases the drag more than the thrust. To achieve a balance between drag and thrust, the swimming velocity must increase significantly so that the thrust is large enough to equal the drag. For larger h the effect is opposite. Any increase in h causes larger increase in thrust compared to drag. Hence, to achieve drag-thrust balance the swimming velocity needs to change only slightly.

2) The analytic solution leads to a critical height h_c at which the swimming velocity is zero (Figure 7b). The analytic solution is not valid for this and smaller heights because the drag-thrust split model for the fin force is not accurate. The swimming velocities at fin heights below the critical value, computed

from self-propulsion simulations, are very small indicating inefficient swimming, i.e., large COT. Thus, optimal swimming conditions do not fall within this regime. We do not present these data because the numerical accuracy was not sufficient to report them quantitatively. It was computationally expensive for us to explore this regime because very refined meshes are required in this case to resolve the flow due to a tiny ribbon fin attached to a large plate.

S2.2 Cost of transport (COT)

To understand the COT trends we first consider the trend of average power plotted in Fig. 7a. It is seen that the data fit a single curve that scales as h^3 over the entire range. It is found from our computations that the power is dominated by the work done to flap the ribbon fin laterally. The velocity V_w of lateral motion is maximum at the bottom edge of the ribbon fin and scales as $h\theta_{\max}f$. Thus, the power is expected to scale as $\rho V_w^3 A$, where A is some scale for area. The power spent is not substantially influenced by the swimming velocity for the scenarios considered here. Our computations also show that the dominant contribution to power spent from lateral flapping comes from the bottom edge of the fin. Thus, the appropriate scale for A is not expected to depend strongly on h . Therefore, it follows that power $P \sim h^3$, consistent with Figure 7a.

To compute the COT analytically we use the curve fit for power in Fig. 7a and divide it by the analytically obtained swimming velocity (equation S8). This is plotted in Fig. 7c and compared with the COT computed from self-propulsion simulations. The agreement is found to be good.

The analytic solution helps to better understand the trend in $\text{COT} = P/U_s$ above the critical fin height. Since the swimming velocity changes faster with respect to h at lower values of h , it compensates for the h^3 rise of power. This gives the low and nearly constant trend of COT with respect to h in the simulation data. At larger h the swimming velocity increases with respect to h at a rate that is less than h^3 . Hence, $\text{COT} = P/U_s$ increases with respect to h , thus, making swimming with a larger fin less and less effective. As noted before, the variation in the swimming velocity can be understood in terms of different scalings, with respect to h , of the drag and thrust of the ribbon fin. Therefore, the key factors that explain the trends in COT with respect to the fin height are the different mechanisms of drag and thrust on the ribbon fin.

S2.3 Effect of a realistic fish body drag

In case of the idealized plate-fin swimmer, the plate drag is dominated by boundary layer flow and scales as $U^{3/2}$. In case of an actual fish, this may not be an accurate drag estimate due to the presence of form drag on the body. To ensure that the key features obtained in the idealized plate-fin model are not affected by this factor, we consider an analytic solution with a different body drag. To that end, we replace the plate drag term $CU^{3/2}$ in equation S7 with EU^2 , which represents the typical pressure drag scaling at high Reynolds numbers. Our prior simulations for the drag force on a realistic CAD model of the body of a black ghost knifefish [4], give $E = 0.055 \text{ mN}\cdot\text{s}^2/\text{cm}^2$. Using this drag model for the body we find the analytic solution for the swimming velocity. Then we estimate the COT for the body-fin assembly by assuming that the primary contribution to power comes from the fin – which was verified in the plate-fin case. To obtain COT, we use the same power curve as that in Fig. 7a and divide it by the analytically calculated swimming velocity based on the body drag model. Fig. 7c shows a comparison between the COT for the plate-fin and body-fin assemblies. The key features pertaining to the minimum in COT are the same. Thus, all the trends discussed above about optimal fin height are applicable even with a realistic body drag.

S3 Sensitivity of COT to perturbations in plate height

We measured the body and the fin height of 13 species from 8 genera of South American weakly electric fishes in the family Apterontidae (see Section and Table 3). We found that the mean body height, at mid-fin length, was 1.86 cm with a standard deviation of 0.85 cm. The mean fin height, at mid-fin length, was measured to be 0.97 cm. This is within the range our prediction for optimal fin height. Although the standard deviation of the fin height is as high as 0.84 cm, the measured fin height does not vary significantly. The standard deviation of fin height is 0.33 cm.

In this section we investigate how sensitive the COT trend is to variations in plate height. Note that the COT trend is the one that leads to the prediction of the fin height. For this, holding the fin height constant, we first find the rate of change of swimming speed with plate height using equation S8. The rate of change of velocity is then used to find the change in cost of transport due to perturbations in plate height. The change in cost of transport will provide insights into how optimal fin height will change with plate height.

The rate of change of swimming velocity with plate height, after differentiating equation S8 at constant fin height, is given by

$$\frac{\partial U_s}{\partial s} = -\frac{C'U^{3/2}}{B} \left[\frac{B(2A_1(U_w - U_s) + A_2)}{(A_1(U_w - U_s)^2 + A_2(U_w - U_s))^2} + \frac{3C\sqrt{U_s}}{2B} \right], \quad (\text{S9})$$

where $C' = \partial C/\partial s$. The drag on the plate has a linear dependence on the plate height. Consequently, C will also have a linear dependence on plate height. We find $C' = \partial C/\partial s = 0.0085 \text{ mN}\cdot\text{s}^{3/2}/\text{cm}^{3/2}$.

The rate of change of cost of transport is found by taking the derivative of P/U_s with respect to s at constant fin height. It is given by

$$\frac{\partial COT}{\partial s} = -\frac{COT}{U_s} \frac{\partial U_s}{\partial s}. \quad (\text{S10})$$

The change in cost of transport, ΔCOT , due to a perturbation in plate height, Δs , is computed using the above equation. This is used to estimate the change in the computed value of the cost of transport corresponding to the standard deviation of the measured body height of fishes. These estimated changes are plotted in Figure 7. It is seen that although the plate height does vary, the corresponding variation in COT is very small at small fin height h , while at larger values of h the change is moderate. In short, the basic trend of the COT with fin height is unaltered by changes to the plate height.

S4 Navier-Stokes equation

The Navier-Stokes equation for incompressible flow

$$\frac{\partial \mathbf{u}}{\partial t} + (\mathbf{u} \cdot \nabla) \mathbf{u} = -\frac{1}{\rho} \nabla p + \nu \nabla^2 \mathbf{u}, \quad (\text{S11})$$

where \mathbf{u} is the fluid velocity, p is the pressure, ν is the kinematic viscosity of the fluid, and ρ is the fluid density. The second term on the left-hand-side is the nonlinear inertia term referred to in the Manuscript.

References

1. Lighthill, J. *Mathematical biofluidynamics* (SIAM, Philadelphia, PA, 1975).

2. Lighthill, J. Large-amplitude elongated-body theory of fish locomotion. *Proc. Roy. Soc. B.* **179**, 125–138 (1971).
3. Lighthill, J. & Blake, R. Biofluidynamics of balistiform and gymnotiform locomotion 1. Biological background, and analysis by elongated-body theory. *J. Fluid Mech.* **212**, 183–207 (1990).
4. MacIver, M. A., Shirgaonkar, A. A. & Patankar, N. A. Energy-information trade-offs between movement and sensing. *PLoS Comput. Biol.* **6** (2010).